Chinese Chemical Letters 34 (2023) 107355

Contents lists available at ScienceDirect

Chinese Chemical Letters

journal homepage: www.elsevier.com/locate/cclet

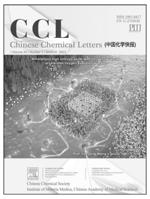

# Modulation of ionic arrangement in polar magnet by chemical pressure

Shuang Zhao[a], Jinjin Yang[a], Yifeng Han[a,*], Meixia Wu[b], Man-Rong Li[a,*]

[a] Key Laboratory of Bioinorganic and Synthetic Chemistry of Ministry of Education, School of Chemistry, Sun Yat-sen University, Guangzhou 510006, China
[b] Institute of Semiconductors, Guangdong Academy of Sciences, Guangzhou 510650, China

ARTICLE INFO

*Article history:*
Received 23 February 2022
Revised 13 March 2022
Accepted 18 March 2022
Available online 21 March 2022

*Keywords:*
Chemical pressure
Trapping metastable-phase
Cationic arrangement
Antiferromagnetism
Dielectricity

ABSTRACT

The similarity of local structure-connection pattern and volumetrically compressive strain between host and guest phases can be used to stabilize heteroid metastable matter and tune the local structure and properties. Here a series of metastable $ABO_3$ ($A = $ Mn; $B = $ Mn$_{0.5}$Mo$_{0.5}$, Mn$_{1/3}$Ta$_{2/3}$, and Mn$_{0.5}$Ta$_{0.5}$) were trapped in LiTaO$_3$ to form solid-solutions, where the difference of solid solubility limit reveals the barrier of size effect on chemical pressure. All samples show antiferromagnetic characters, in which the (LiTaO$_3$)$_{1-x}$-[Mn(Mn$_{0.5}$Mo$_{0.5}$)O$_3$]$_x$ series exhibit more complex magnetic and dielectric behaviors with the increasing of metastable guest phase, stemming from the complex interactive mechanism between Mn$^{2+}$ and Mo$^{6+}$. The cell parameter variation of (LiTaO$_3$)$_{1-z}$-[Mn(Mn$_{0.5}$Ta$_{0.5}$)O$_3$]$_z$ shows a more regularly changing tendency, on account of the smallest size barrier. These findings show that chemical pressure can effectively stimulate the physical pressure to intercept and modulate a metastable phase at atomic-scale by compressibility effect between like structures at ambient pressure.

Corundum-related polar oxides exhibit a lot of appealing physical characters in transition-metal enriched systems [1–3]. However, the number of double corundum-related polar magnets is very limited compared to chemical-space predictions [4], and thus worthy of further exploration. There a key issue is to lower the synthesis pressure of these materials and reduce the cost in a scaled-up manner, to meet the ultimate goal for practical applications. Stabilization of the high pressure (HP) phase in an isostructural or structurally related matrix by chemical pressure has been proven to be feasible [5–9]. Recently, the LiNbO$_3$ (LN)-type Mn$_2$FeNbO$_6$ has been stabilized in LN matrix by forming a solid-solution [9]. Mn$_2$FeNbO$_6$ prepared at high-pressure and high temperature (HPHT, 7 GPa and 1573 K) crystallizes in LN-type $R3c$ with disordered arrangement of Fe and Nb, namely Mn(Fe$_{0.5}$Nb$_{0.5}$)O$_3$ [10]. It is antiferromagnetic (AFM) below 90 K with short-range magnetic ordering up to 200 K, and demonstrates pyroelectric response at lower temperature. However, the Mn$_2$FeNbO$_6$ product is only around 20 mg/batch at 7 GPa in our multi-anvil press. Chemical pressure can dissolve 18% of the HP-Mn(Fe$_{0.5}$Nb$_{0.5}$)O$_3$ in a LN matrix at ambient pressure (AP) in our previous studies [9]. While at 5 GPa, the HP-phase dominated (57%) LN-Mn$_2$FeNbO$_6$ solid solution can be obtained in gram level, which indicates that the assistance of external physical pressure favors stabilization of more HP-phase [9]. The interception of Mn$_2$FeNbO$_6$ in isostructural LN-host significantly modifies the local structure, resulting in enhanced magnetic interactions. The solid-solution exhibits magnetostriction-induced irreversible lattice evolution around the magnetic transition temperatures, showing ferromagnetic (FM) transitions between 516 K and 554 K [9]. These findings show that chemical pressure and the integration of chemical and physical pressure between isostructural compounds are an effective method to decrease the synthetic pressure for metastable phase prepared at HPHT [9,11,12], and further enhance the desired material function by local structure modulation.

Previous research indicates that Mn$_2$MnMoO$_6$ ($R3$, prepared at 8 GPa), a new transitional-metal-only polar corundum oxide, shows interesting magnetism with two magnetic transitions, a large spontaneous polarization, and semiconductor behavior [13]. Unlike Mn$_2$MnMoO$_6$, Mn$_4$Ta$_2$O$_9$ [Mn$_2$(Mn$_{2/3}$Ta$_{1/3}$)TaO$_6$] displays different local structural connection style and magnetodielectric coupling in the AP phase ($P\bar{3}c1$), and diversity of structure and characters under additional pressure, partially owing to the larger ionic size of 5d$^0$ Ta$^{5+}$(0.64 Å) than that of 4d$^0$ Mo$^{6+}$ (0.59 Å) [14–16]. Mn$_2$MnTaO$_6$, a predicted but unreported HP phase [4], is expected to adopt the LN-structure similar to Mn$_2$FeTaO$_6$ ($R3c$) [10], but demonstrates different local structure and valence states compared

---

* Corresponding authors.
*E-mail addresses:* hanyf26@mail.sysu.edu.cn (Y. Han), limanrong@mail.sysu.edu.cn (M.-R. Li).

https://doi.org/10.1016/j.cclet.2022.03.078

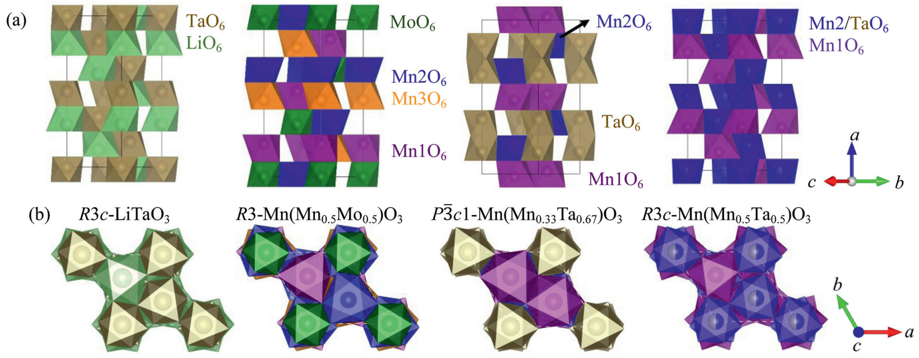

**Fig. 1.** The comparison of crystal structure between host phase $LiTaO_3$ and guest phase [$Mn(Mn_{0.5}Mo_{0.5})O_3$, AP-$Mn(Mn_{0.33}Ta_{0.67})O_3$, $Mn(Mn_{0.5}Ta_{0.5})O_3$]. (a) The crystal structure diagram for host and guest phase, (b) viewed along the crystallographic *c*-axis. The chemical formula of cationic ordered $Mn_2BB'O_6$ phases are written as $Mn(B_{0.5}B'_{0.5})O_3$ for a better comparison with the structure of host $LiTaO_3$, instead of the $B/B'$-disordering representation.

to $Mn_4Ta_2O_9$. Clearly, the crystal structures and physical properties of these $Mn_2BB'O_6$ are strongly related to the coordinated environment (atomic-scale local structure) and valance of magnetic ions (electronic structure), providing an ideal platform for chemical-pressure induced phase interception and modification. In this work, chemical pressure was applied to stabilize the HP forms of $Mn_2MnMoO_6$, $Mn_4Ta_2O_9$, and $Mn_2MnTaO_6$ at AP to reveal the competitions between cationic order-disorder degree and chemical and physical pressures, and investigate the diversity of characters with different interaction between ions. Hence, a suitable host phase is crucial.

As shown in Fig. 1, the connection modes of $LiTaO_3$, $Mn_2MnMoO_6$, AP-$Mn_4Ta_2O_9$, and predicted $Mn_2MnTaO_6$ show certain similarities, where the octahedra are edge- and face-sharing between intralayer and interlayers, respectively, and form honeycomb layered arrangements in the *ab*-plane. However, the cationic ordering degree is in great difference for those compounds. For example, unlike the two crystallographically cationic positions ordered into four and three Wyckoff sites, respectively. The *B*-sites for theoretical $Mn_2MnTaO_6$ are expected to be disordered in LN-type polymorph due to the second order Jahn-Teller effect of $d^0$-$Ta^{5+}$ [10]. Compared with three candidate compounds, the simple-corundum $LiTaO_3$ not only has similar octahedral connection pattern, but also owns smaller cell dimensions ($a = 5.1546(4)$ Å, $c = 13.7799(13)$ Å, $V = 317.08(6)$ Å$^3$) due to the ionic radius difference between octahedrally coordinated $Mn^{2+}$ (0.83 Å, high spin, HS) and $Li^+$ (0.726 Å) [16]. Thus, the volumetrically compressive strain/stress effect on these materials inside a $LiTaO_3$ matrix, which is believed to be equivalent to exerted physical (mechanical) pressure [9,11], is expected to stabilize $Mn_2MnMoO_6$, $Mn_4Ta_2O_9$ and $Mn_2MnTaO_6$ (hereafter redefined as $Mn(Mn_{0.5}Mo_{0.5})O_3$, $Mn(Mn_{0.33}Ta_{0.67})O_3$ and $Mn(Mn_{0.5}Ta_{0.5})O_3$ in $ABO_3$ form for better comparison), and tune their physical characteristics by regulating the cationic order degree in solid solutions. The solid state solutions of $(LiTaO_3)_{1\text{-}x}$-$[Mn(Mn_{0.5}Mo_{0.5})O_3]_x$, $(LiTaO_3)_{1\text{-}y}$-$[Mn(Mn_{0.33}Ta_{0.67})O_3]_y$ and $(LiTaO_3)_{1\text{-}z}$-$[Mn(Mn_{0.5}Ta_{0.5})O_3]_z$ are presented by **LM1**, **LM2** and **LM3**, respectively, for succinct description. Fig. S1 (Supporting information) presents the powder x-ray diffraction (PXD) patterns of $LiTaO_3$-$ABO_3$ synthesized at AP, where the main peaks of all samples can be well indexed with $R3c$ symmetry, suggesting the absence of cationic ordering at $B/B'$-site2, otherwise, a double-corundum $R3$ structure would be formed [4]. $Mn^{2+}(Mn_{0.33}{}^{2+}Ta_{0.67}{}^{5+})O_3$ and $Mn^{2+}(Mn_{0.5}{}^{3+}Ta_{0.5}{}^{5+})O_3$ can be stabilized/dissolved by $LiTaO_3$ up to 50%, higher than that of $Mn^{2+}(Mn_{0.5}{}^{2+}Mo_{0.5}{}^{6+})O_3$ at 30%, which can be attributed to the average *B*-site ionic radius deviation ($\Delta B$): $\Delta B[Mn(Mn_{0.5}Ta_{0.5})O_3] = 0.0025$ Å, $\Delta B[Mn(Mn_{0.33}Ta_{0.67})O_3] = 0.063$ Å, and $\Delta B[Mn(Mn_{0.5}Mo_{0.5})O_3] = 0.12$ Å. Here $\Delta B$ is defined as:

$$\Delta B = \Sigma \frac{|(r(G) - r(Q))|}{n} \tag{1}$$

where $r(G)$ and $r(Q)$ are the *B*-site radii of guest and matrix material, respectively, $n$ represents the number of *B*-site atoms. Here, $r(G)$ denotes $r(Ta^{5+}) = 0.64$ Å, $r(Mn^{3+}$, HS$) = 0.645$ Å, $r(Mn^{2+}$, HS$) = 0.83$ Å and $r(Mo^{6+}) = 0.59$ Å; $r(Q) = r(Ta^{5+}) = 0.64$ Å at octahedral surrounding [16].

In the obtained $LiTaO_3$-$ABO_3$ solid solutions, the *B*-site Mn, Ta and Mo are randomly distributed as $Mn(Mn_{0.33}Ta_{0.67})O_3$, $Mn(Mn_{0.5}Ta_{0.5})O_3$ and $Mn(Mn_{0.5}Mo_{0.5})O_3$ in the $LiTaO_3$ matrix. The peak shifts toward lower angle compared with those of $LiTaO_3$ with the increase of *x*, *y* and *z* as observed in Fig. S1, which illustrate the expansion of cell volume and successful formation of solid solution, originated from the larger ionic radius of $Mn^{2+}$ (0.83 Å, HS) than that of $Li^+$ (0.76 Å) at the *A*-site, and comparable ionic size between $Ta^{5+}$ and $Q^{\sim 4+}$. Fig. 2, Figs. S2 and S3 (Supporting information) display the Rietveld refinement plots of a series of AP-made $LiTaO_3$-$ABO_3$. Detailed crystallographic parameters and structural information are listed in Tables S1–S3 (Supporting information). $Li_{1.6}Mn_{2.2}Mo_3O_{12}$ (*Pnma*) related impurity [17] appears to be around 8.90(1) and 6.23(2)% for **LM1** at $x = 0.3$, 0.4, respectively. A few unidentified impurities in **LM2** and **LM3** appear at $y = 0.5$ and $z = 0.5$, respectively. HPHT synthesis was thus applied to reduce the impurity of **LM1** with $x = 0.3$ and 0.4 from 1 to 3 GPa, and further raise the solid solution limit of the HP component as applied in $LiNbO_3$-$Mn_2FeNbO_6$ system [9]. Surprisingly, the additional physical pressure did not improve the purity for **LM1** (Fig. S4 in Supporting information) as expected, implying that the cooperation of chemical and applied physical pressure is not enough to overcome the size/charge effect, namely the difference of ionic radius and charge between cations to cause ionic ordering. Figs. S5a–c (Supporting information), respectively shows the *x*, *y* and *z*-dependent cell evolution for $LiTaO_3$-$ABO_3$, where the cell parameters show different variation tendency for different *B*-site ions. For **LM1**, the *c*-axis gradually increases with incremental *x*. In contrast, *a* almost remains constant when *x* increases from 0.2 to 0.3, which suggests that the crystal structure is more elastic along the *c*-axis [18]. As for **LM2**, although the overall cell evolution trend of *V* is similar to that in Fig. S5a, the *a* and *c* show abnormal change at 0.4 and 0.2, respectively, and deviate from the increasing linearity. This is probably due to the suppression from chemical pressure like physical pressure, and change of the spin state of magnetic ion [19]. The variation of cell parameters for **LM3** bears different trend compared with the other two series, in that the *a*, *c* and *V* are nearly linear increasing with enlarged *z*, and roughly follow the Vegard's law [20]. The smallest size difference between $Mn^{3+}$ and

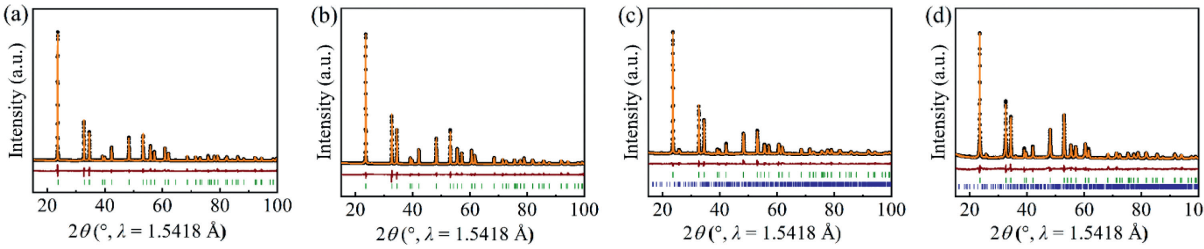

**Fig. 2.** Rietveld refinements of the PXD data for **LM1**: (a) $x=0.1$, (b) $x=0.2$, (c) $x=0.3$, (d) $x=0.4$. Orange line is the observed result, black dots represent the calculated fit, difference is shown as wine line, olive ticks mark the peak positions, the bottom ticks in (c) and (d) mark the position of $Li_{1.6}Mn_{2.2}Mo_3O_{12}$ (*Pnma*, 8.90% and 6.23% for $x=0.3$ and 0.4) [17].

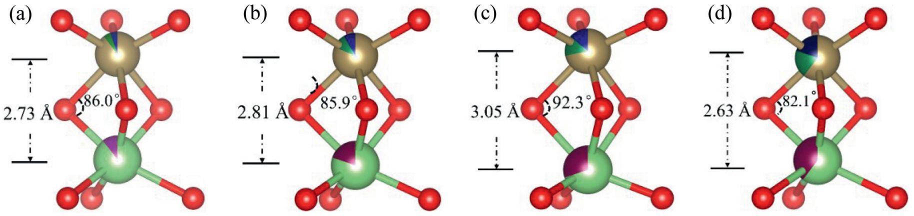

**Fig. 3.** The evolution of $d_{A\text{-}B}$ and angle of *A*-O-*B* for **LM1**: (a) $x=0.1$, (b) $x=0.2$, (c) $x=0.3$, (d) $x=0.4$. Green, wine, dark yellow, navy and olive represent Li, Mn1, Ta, Mn2 and Mo, respectively.

$Ta^{5+}$ at *M*-site in **LM3**, in which similar cell distortion tendency is generated with increasing substitution, is responsible for the different variation trend of lattice parameters to the other two series. The two kinds (three short and three long) of *A*-O distances for $LiTaO_3$-$ABO_3$ are listed in Tables S1–S3 (Supporting information). The $AO_6$ octahedra are very distorted in **LM1**, **LM2** and **LM3** with 10% guest phase, the short and long *A*-O bond lengths are 1.950(20) and 2.232(18) Å, 2.052(14) and 2.363(16) Å, and 2.028(6) and 2.396(11) Å, respectively, giving large octahedral distortion parameters [21]. $\Delta_{Li/Mn1}$ of $45.47\times10^{-4}$, $49.6\times10^{-4}$, and $69.2\times10^{-4}$ due to the low Mn content (10%) at the *A*-site, which is, however, insufficient to affect the overall structural distortion to generate an highly ordered structure than the host phase $LiTaO_3$, as previously reported for $(Li_{1\text{-}x}Mn_x)(Fe_{x/2}Nb_{1\text{-}x/2})O_3$ [9]. As the Mn content increases to $x=0.4$ and $y=0.5$ in **LM1** and **LM2**, the large discrepancy (0.275 and 0.254 Å) between the two kinds of <Li/Mn-O> bond lengths (2.018(19)–2.293(17) Å and 2.003(13)–2.257(14) Å) brings secondary large $\Delta_{Li/Mn1}$ of $40.67\times10^{-4}$ and $35.6\times10^{-4}$, which can be attributed to the fact that, the chemical pressure stabilized crystal structure has reached its solid-solution limit, and the competition between thermodynamic stability and chemical pressure has reached an equilibrium. The $\Delta_{Li/Mn1}$ of **LM3** regularly decreases with the increase of *A*-site $Mn^{2+}$ ions, since that the distortion will move with the hopping of $e_g$ electrons between $Mn^{2+}$ and $Mn^{3+}$, which makes the maximum $\Delta_{Mn2/Ta}$ ($53.4\times10^{-4}$) and minimum $\Delta_{Li/Mn1}$ ($0.9\times10^{-4}$). In addition, it is noticeable that the $BO_6$ octahedra in **LM1** are more regular than those in **LM2** and **LM3**. The difference value between shorter and longer *B*-O bonds gradually decreases from 0.088 Å to 0.033 Å with incremental *x* in **LM1**.

The variation of $d_{A\text{-}B}$ distance between face-sharing $AO_6$-$BO_6$ octahedral pairs along the *c*-axis for **LM1** is shown in Fig. 3, which firstly shows an increasing and then decreasing with *x* from 0.1 to 0.4. As shown in Figs. S6 and S7 (Supporting information), for $LiTaO_3$-$ABO_3$ ($B=Mn_{0.5}Ta_{0.5}$, $Mn_{1/3}Ta_{2/3}$), the *B*-site is occupied by Ta/Mn, the variation of $d_{A\text{-}B}$ exhibits remarkable difference from that in **LM1**. The $d_{A\text{-}B}$ evolution is more regular, decreasing from 3.03 Å to 2.87 Å and 3.05 to 2.91 Å with the substituted ions increase in $B=Mn_{0.5}Ta_{0.5}$, $Mn_{1/3}Ta_{2/3}$, respectively. The lattice parameters for **LM1** and **LM2** show nonlinear evolution in some region, disobeying the Vegard's law [20], due to the larger ionic radius difference at the mixed *B*-site than that in **LM3**. Thereby, it is becoming more difficult to trap $ABO_3$-phase within $LiTaO_3$ and reaches the solid-solubility limit with incremental guest phase, in that the limited chemical pressure is not enough to overcome the size-difference effect to further boost the contents of guest phase.

Although the reported $Mn(Mn_{0.33}Ta_{0.67})O_3$ [14,15] and $Mn(Mn_{0.5}Mo_{0.5})O_3$ [13] are in different space groups from $LiTaO_3$ (*R*3*c*), their local octahedral connection patterns are similar, and only differ in the cationic ordering degree (Fig. 1). Our findings demonstrate that the experimental or theoretical high-pressure phase can be intercepted at AP by solid fusion in host matrix with similar arrangement of local structure motifs rather than strictly isostructural lattices. Here the volumetric difference between $LiTaO_3$ (317.08(2) $Å^3$) and $Mn(Mn_{0.5}Mo_{0.5})O_3$ (*R*3–343.25(1) $Å^3$), and $Mn(Mn_{0.33}Ta_{0.67})O_3$ ($P\bar{3}c$-353.55(1) $Å^3$) reaches 26.16 and 36.47 $Å^3$, respectively, which, together with the mono-*B* site in$LiTaO_3$, generates compressive effect (positive chemical pressure), and induces lattice stress to break the energy barrier between ionic order and disorder and thus stabilize the phases to *R*3*c* at AP. It is noticeable that the chemical pressure, which derives from the volumetric difference between $LiTaO_3$ with one crystallographic *B* site and desired candidate phases with ordered *B*/*B*' sites, prefers to stabilize the phase with short-range random order than long-range order, which is the preference of physical pressure [22]. For $Mn(Mn_{0.5}Ta_{0.5})O_3$, the comparable ionic radius difference at *A*-site and close ionic radius between $Mn^{3+}$ and $Ta^{5+}$ at *B*-site offer an effective chemical pressure to stabilize $Mn(Mn_{0.5}Ta_{0.5})O_3$ in $LiTaO_3$ up to mole ratio of 50%. Understandably, the positive (compressive) chemical pressure exerted on the high-pressure polymorphs equals to the negative (tensile) chemical pressure experienced by $LiTaO_3$. So, in order to evaluate the chemical pressure, which stems from the volumetric difference between $LiTaO_3$ and the solid solutions, the *P*-*V* curves were calculated for $LiTaO_3$ by the Murnaghan equation of state [23] and the detailed results are shown in Fig. S8 (Supporting information), which indicate equivalent pressure up to 3.9 GPa, for example to stabilize **LM3** ($z=0.5$), which further proved the feasible trapping for metastable phase with chemical pressure at AP. The measurements of magnetic and dielectric response were executed to further study the properties with the change of ionic ordered degree modulated under chemical pressure.

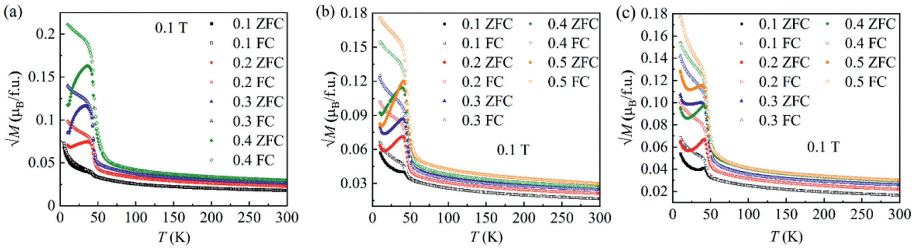

**Fig. 4.** Temperature-dependent sqrt-magnetization of (a) **LM1**, (b) **LM2**, (c) **LM3** in ZFC/FC at 0.1 T between 10 K and 300 K.

Fig. 4 illustrates the variation tendency of temperature-dependent magnetization for $LiTaO_3$-$ABO_3$ series. The zero-field cooled (ZFC) and field cooled (FC) curves for all samples show the like-λ form, which implies the possibility of spin-glass or magnetic competition between FM and AFM phases. The negative Curie-Weiss temperature $\theta$, determined by Curie-Weiss fitting from the 200-300 K data, demonstrates that all samples are AFM dominated. The detailed magnetic parameters are listed in Tables S4–S6 (Supporting information). It is noticeable a nonlinear change of $T_N$ between 33.4–37.7 K, 39.2–41.1 K and 38.2–41.1 K for $B = Mn_{0.5}Mo_{0.5}$, $Mn_{0.33}Ta_{0.67}$, and $Mn_{0.5}Ta_{0.5}$, respectively. For **LM1** and **LM2**, compared with the reported guest phases $Mn(Mn_{0.5}Mo_{0.5})O_3$ and AP-$Mn(Mn_{0.33}Ta_{0.67})O_3$, the change of cationic arrangement directly modifies the magnetic interactions between $Mn^{2+}$-$O^{2-}$-$Mn^{2+}$. The increased disordered degree and lower content of magnetic ions induce local structural relaxation and weaken magnetic interaction between ions. Hence, the magnetic transition at 19 K rooted in the *A*-sublattice $Mn^{2+}$ in $Mn(Mn_{0.5}Mo_{0.5})O_3$ disappears in **LM1**. The magnetic transitions in **LM1** and **LM2** are lower than those in $Mn(Mn_{0.5}Mo_{0.5})O_3$ and AP-$Mn(Mn_{0.33}Ta_{0.67})O_3$ from 47 K and 102 K to 33.4–37.7 K and 39.2–41.1 K, respectively.

The nearest interlayer Mn distance, bond angle of Mn-O-Mn, and the change of $MnO_6$ octahedral distortion accompanied with anomalous lattice parameter variation, are the inducement of $T_N$ change. The variation of $\theta$ of **LM1** first increases and then decreases with *x* increasing. In contrast, the $\theta$ evolution behaviors of **LM2** and **LM3** behave oppositely. The competition between AFM and FM directly reflects the $\theta$ value, where the dominance of AFM interactions leads $\theta$ decreasing and *vice versa*. The growth of disordered degree between ions of unlike elements enhances the complexity of magnetic interaction to strengthen the frustration [24,25]. **LM2** owns a relatively lowest magnetic frustration *f* (defined as $|\theta|/T_N$) than those of the other two systems, as the lowest content of Mn ions in *B*-site will weaken the strength of magnetic interactions between different atomic sites. The calculated $\mu_{eff}$ values *via* all site HS-$Mn^{2+}$ and HS-$Mn^{2+}$(*A*-site)/HS-$Mn^{3+}$(*B*-site) of **LM1** (HS-$Mn^{2+}$), **LM2** (HS-$Mn^{2+}$) and **LM3** [HS-$Mn^{2+}$(*A*-site), HS-$Mn^{3+}$(*B*-site)], respectively, are lower than the theoretical values because of the frustration between magnetic lattice and ionic disorder [26].

Isothermal magnetization curves for $LiTaO_3$-$ABO_3$ are illustrated in Figs. S9–S11 (Supporting information). The FM component obviously exists in all samples at low temperature region. The hysteresis loops of isothermal magnetization gradually emerge at 10 K, due to the enhancement of magnetic phase competition with enriched magnetic ions. Nevertheless, the AFM interactions are still dominant. Above $T_N$, the isothermal magnetization plots exhibit abnormal variations when the metastable guest phases reach ultimate values for **LM1** and **LM2**. The isothermal curves of **LM1** ($x = 0.4$) and **LM2** ($y = 0.5$) deviate linearity and exhibit a hysteresis loop at 50 and 45 K, respectively, indicating weak interactions of short-range magnetic ordering or canting AFM.

The temperature-dependent relative dielectric constants ($\varepsilon_r$) and dielectric loss (tan$\delta$) at different frequencies without field for selected **LM1** ($x = 0.4$) are illustrated in Fig. S12a (Supporting information). The $\varepsilon_r$ increases from 17.5 to 18.5 from 10 K to 200 K, which almost remains constant at different frequencies and shows a weak dependence on temperature and frequencies. The tan$\delta$ plot also exhibits a weak temperature correlation at the same temperature range, where the electrodes induce a large loss at 1 MHz than at low frequencies. These phenomena derive from the strengthened restraint of cooperation conversion between local electric polarization as the *A*- and *B*-site ions are disorderedly aligned [27], which induce the absence of platform in the curves of $\varepsilon_r$ dependent *T* as same as in $Mn(Mn_{0.5}Mo_{0.5})O_3$ [13]. At the low disorder degree and relative weak restraint effect, the $\varepsilon_r$ values of **LM2** ($y = 0.4$) and **LM3** ($z = 0.4$) show relatively clear differences, which are about 4 and 6 between 10 K and 200 K. However, the charge thermal motion is motivated and leads a significant increase for $\varepsilon_r$ with a divergence in frequency with *T* increasing for all selected samples. Besides, the dielectric relaxation of **LM1** ($x = 0.4$) can be observed near room temperature in Fig. S12a (bottom), which may be from the polarization difference because of the charge thermal motion. The dielectric relaxation phenomenon of **LM2** ($y = 0.4$) and **LM3** ($z = 0.4$) occur at *T* about 40 K, which is much lower than that in **LM1**, as the weak polarization-temperature dependency with frequencies changing. Figs. S12a and S13a (Supporting information) demonstrate the temperature-dependence of $\varepsilon_r$ at different additional magnetic field for **LM1** and **LM2**. No anomalous dielectric peaks are observed around the magnetic transition temperatures under additional field, and the permittivity hardly changes over the test ranges with and without field, indicating the absence of magneto-electric and dielectric coupling.

The real part permittivity $\varepsilon'$ and imaginary part of dielectric permittivity ($\varepsilon''$) with frequency at selected temperatures are measured for selected samples as illustrated in Figs. S12–S14 (Supporting information). The $\varepsilon'$ values of all samples show more obvious frequency dependence with temperature increase, and the $\varepsilon'$ values decrease with increasing frequency. The $\varepsilon''$ of **LM1** ($x = 0.4$) appears two frequency dependent variation trends around 250 K as dividing line. Above 250 K, where dielectric relaxation occurs, the platform-like area appears and shifts to high frequency region. For **LM2** ($y = 0.4$) and **LM3** ($z = 0.4$), the $\varepsilon''$ exhibits similar variation from 10 K to relaxation peak of high-frequency about 90 K, then changes from negative to positive correlation with frequency. The tan$\delta$ *vs.* frequency curves are displayed in Figs. S15a–c (Supporting information). According to the relationship between tan$\delta$ and frequency, a linear fitting was performed with Arrhenius relation $f = f_0\exp(-E_a/k_BT)$ [28], where $f_0$ is the frequency factor, $E_a$ is the activation energy and $k_B$ is the Boltzmann constant. As shown in the insets, the fitting results for **LM1** ($x = 0.4$), **LM2** ($y = 0.4$) and **LM3** ($z = 0.4$) are $E_a$ = 0.44, 0.022, 0.027 eV and $f_0$ = $6.97 \times 10^{11}$, $3.2 \times 10^6$, $6.9 \times 10^6$ Hz, respectively. The higher $E_a$ of **LM1** than $Mn(Mn_{0.5}Mo_{0.5})O_3$ [13] demonstrates the inducement of relaxation from ions hopping to the difference of polarization at boundaries and strengthened interaction between polarons. However, the relaxation for other selected samples derives from the electron transfer between magnetic ions.

In summary, the polar *R*3*c*-$LiTaO_3$ is used as a matrix to stabilize a series of high-pressure metastable polar and magnetic polymorphs of $Mn(Mn_{0.5}Mo_{0.5})O_3$, $Mn(Mn_{0.33}Ta_{0.67})O_3$ and $Mn(Mn_{0.5}Ta_{0.5})O_3$ by chemical pressure in solid solution. The volumetric difference and likely local structural patterns between $LiTaO_3$ and targeted high-pressure phases are beneficial to modify the cationic ordering degree and introduce magnetic competition between ferromagnetic and antiferromagnetic interactions. The solid solution limitation performs a significant difference among three series due to the ionic size and electronic structure effect among different compounds. The structural modulation influences the magnetic interaction and change the magnetic ordering temperature and frustration. The dielectric behaviors indicate that both the *A* and *B*-site atomic substitutions, which contain strong spin orbit coupling ions, can significantly affect the dielectric relaxation mechanism and the interaction between polar clusters. These discoveries proposed a feasible way to trap metastable high-pressure phase in a like-matrix by chemical pressure, and thus tune the physical properties and soften the synthesis conditions in a cost-effective way to significantly scale up the metastable products.

## Declaration of competing interest

The authors declare that they have no known competing financial interests or personal relationships that could have appeared to influence the work reported in this paper.

## Acknowledgments

This work was financially supported by the National Natural Science Foundation of China (NSFC, Nos. 21875287, 22090041, 22105228 and 11804404), the China Postdoctoral Science Foundation (No. 2021M693603).

## Supplementary materials

Supplementary material associated with this article can be found, in the online version, at doi:10.1016/j.cclet.2022.03.078.

## References

[1] H.L. Feng, C.J. Kang, B. Kim, et al., Chem. Mater. 33 (2021) 6522–6529.
[2] M.R. Li, E.E. McCabe, P.W. Stephens, et al., Nat. Commun. 8 (2017) 2037.
[3] S. Chaudhary, P. Srivastava, S.D. Kaushik, V. Siruguri, S. Patnaik, J. Magn. Magn. Mater. 475 (2019) 508–513.
[4] G.H. Cai, M. Greenblatt, M.R. Li, Chem. Mater. 29 (2017) 5447–5457.
[5] J.M. Fournier, Phys. B: Condens. Matter. 190 (1993) 50–54.
[6] N.M. Dawley, E.J. Marksz, A.M. Hagerstrom, et al., Nat. Mater. 19 (2020) 176–181.
[7] A. Aimi, D. Mori, K.I. Hiraki, et al., Chem. Mater. 26 (2014) 2601–2608.
[8] T. Katsumata, C. Ohba, A. Tobe, et al., Chem. Lett. 47 (2017) 37–39.
[9] Y. Han, C.H. Zhu, Y. Peng, et al., Chem. Mater. 32 (2020) 1618–1626.
[10] M.R. Li, D. Walker, M. Retuerto, et al., Angew. Chem. Int. Ed. 52 (2013) 8406–8410.
[11] Y.L. Ma, M.S. Molokeev, C.H. Zhu, et al., J. Mater. Chem. C 8 (2020) 5082–5091.
[12] E. Solana-Madruga, Y. Sun, A.M. Arevalo-Lopez, J.P. Attfield, Chem. Commun. 55 (2019) 2605–2608.
[13] S. Zhao, J.J. Yang, Y.F. Han, et al., Chem. Mater. 34 (2022) 1930–1936.
[14] N. Narayanan, A. Senyshyn, D. Mikhailova, et al., Phys. Rev. B 98 (2018) 134438.
[15] E. Solana-Madruga, C. Ritter, O. Mentré, Á.M. Arévalo-López, J. Mater. Chem. C 9 (2021) 14916–14920.
[16] R.D. Shannon, Acta Cryst. A 32 (1976) 751–767.
[17] S.F. Solodovinkov, Z.A. Solodovnikova, R.F. Klevtsova, et al., J. Struct. Chem. 35 (1994) 871–878.
[18] M.R. Li, M. Retuerto, P.W. Stephens, et al., Angew. Chem. Int. Ed. 55 (2016) 9862–9867.
[19] F. Aguado, F. Rodriguez, P. Núñez, Phys. Rev. B 76 (2007) 094417.
[20] A.R. Denton, N.W. Ashcroft, Phys. Rev. A 43 (1991) 3161–3164.
[21] I.D. Brown, R.D. Shannon, Acta Cryst. A 29 (1973) 266–282.
[22] S. Vasala, M. Karppinen, Prog. Solid State Chem. 43 (2015) 1–36.
[23] V.G. Tyuterev, N. Vast, Comput. Mater. Sci. 38 (2006) 350–353.
[24] L.T. Nguyen, M. Saubanère, Q. Zhang, R.J. Cava, Chem. Mater. 33 (2021) 600–607.
[25] O. Mustonen, S. Vasala, E. Sadrollahi, et al., Nat. Commun. 9 (2018) 1085.
[26] E. Solana-Madruga, K.N. Alharbi, M. Herz, P. Manuel, J.P. Attfield, Chem. Commun. 56 (2020) 12574–12577.
[27] J. Deng, F. Han, B. Schwarz, et al., Inorg. Chem. 60 (2021) 6999–7007.
[28] H. Li, L. Wang, Y. Zhu, P. Jiang, X. Huang, Chin. Chem. Lett. 32 (2021) 2229–2232.